

# Finite Element Simulation of Pinched Pressure-Driven Flow Injection in Microchannels

Xiaoxia Bai, Jacques Josserand, Henrik Jensen, Joël S. Rossier, and Hubert H. Girault\*

Laboratoire d'Electrochimie Physique et Analytique, Institut de Chimie Moléculaire et Biologique, Ecole Polytechnique Fédérale de Lausanne, 1015 Lausanne, Switzerland

**A pinched pressure-driven flow injection on a microchip is numerically simulated in order to optimize the relative values of the operational parameters. The geometry studied is a two-dimensional rectangular channel featuring a cross-junction with a large depth-over-width ratio. The hydrodynamic and convection-diffusion equations are solved for the two steps of the process: first, the sample solution is pinched into the transversal channel (injection channel), and then it is injected into the longitudinal one (separation channel), where the time evolution of the concentration is analyzed for different types of the detectors. Electroosmotic flow calculations have also been performed and have shown a good agreement with literature. The results for pressure-driven flow point out that the shape of the detection signal is strongly dependent on the velocity in the separation channel and on the position of the detection probes. The so-called double-humped peak, caused by the parabolic flow profile at high driving flow rate is analyzed. A tight pinch greatly decreases the amount of injected sample and, consequently, the signal sensitivity without increasing its quality. A proper pullback of the sample during the separation process can decrease the tailing due to the sample leakage from the injection channel. Although a high sample pullback causes a considerable decrease in the signal sensitivity, it also greatly enhances the peak resolution. Finally, it is shown that a wider injection channel with high sample pullback ensures an improved signal sensitivity with good resolution.**

Micro total analysis systems ( $\mu$ -TASs) refers to analytical systems of micrometer or smaller dimensions that contain all the necessary components for analysis. The microchips, which constitute the central part of  $\mu$ -TASs, are usually made of glass, silica, or a polymeric substrate. Among all the experimental stages in  $\mu$ -TAS, the injection of a sample plug is a critical step that affects the separation and the detection. Most studies reported in the literature are dedicated to the electrokinetic injection method.<sup>1,2</sup>

In general,<sup>3</sup> one of the main advantages of this technique is the flat laminar flow profile (no distortion of the sample plug) that is favorable for analytical purposes. Nevertheless, it requires well-defined and stable chemical properties of both the channel wall and the fluid solution.<sup>4,5</sup> Pressure-driven flow injection<sup>6–9</sup> is much less used in microsystems because of the large dispersion of the injected sample plug. This fact is due to the parabolic profile of the flow, inducing a velocity of the fluid that is lower near the walls than in the center of the channel. However, a notable advantage of the pressure-driven injection is that it is independent of most of the properties of both the solutions and the microchip materials. Therefore, the implementation of this injection technique in  $\mu$ -TASs could be a favorable way to deal with complex mixtures. For example, this pinch injection method can be coupled with micro-liquid chromatography and capillary electrochromatography.

To control the amount of injected sample, many methods have been developed, such as pinched injection<sup>10</sup> and gated injection<sup>11</sup> on T and double-T geometries as well as cross-junctions, but mainly in an electrophoretic or an electrokinetic injection mode.

Numerical simulations can be a great help in the design and optimization of microsystems. Simulations of electrokinetic flows<sup>12,13</sup> and injection in microsystems<sup>14,15</sup> have been carried out. The experimental results are usually well-explained, and some constructive suggestions for experimental designs have been highlighted. For example, the simulations suggest that the tightest

\* Phone: +41 21 693 31 51. Fax: +41 21 693 36 67. E-mail: hubert.girault@epfl.ch.

(1) Harrison, D. J.; Manz, A.; Fan, Z.; Ludi, H.; Widmer, H. M. *Anal. Chem.* **1992**, *64*, 1926–1932.

(2) Seiler, K.; Harrison, D. J.; Manz, A. *Anal. Chem.* **1993**, *65*, 1481–1488.

(3) Herr, A. E.; Molho, J. I.; Santiago, J. G.; Mungal, M. G.; Kenny, T. W.; Garguilo, M. G. *Anal. Chem.* **2000**, *72*, 1053–1057.

(4) Alarie, J. P.; Jacobson, S. C.; Ramsey, J. M. *Electrophoresis* **2001**, *22*, 312–317.

(5) Crabtree, H. J.; Cheong, E. C. S.; Tilroe, D. A.; Backhouse, C. J. *Anal. Chem.* **2001**, *73*, 4079–4086.

(6) Kutter, J. P. *TrAC, Trends Anal. Chem.* **2000**, *19*, 352–363.

(7) Fu, C. G.; Fang, Z. L. *Anal. Chim. Acta* **2000**, *422*, 71–79.

(8) Xu, Y.; Bessoth, F.; Manz, A. *Chin. J. Anal. Chem.* **2000**, *28*, 876–878.

(9) Bruin, G. J. M. *Electrophoresis* **2000**, *21*, 3931–3951.

(10) Jacobson, S. C.; Hergenroder, R.; Koutny, L. B.; Warmack, R. J.; Ramsey, J. M. *Anal. Chem.* **1994**, *66*, 1107–1113.

(11) Jacobson, S. C.; Hergenroder, R.; Moore, A. W.; Ramsey, J. M. *Anal. Chem.* **1994**, *66*, 4127–4132.

(12) Molho, J. I.; Herr, A. E.; Kenny, T. W.; Mungal, M. G.; St. John, P. M.; Garguilo, M. G.; Paul, P. H.; Deshpande, M.; Gilbert, J. R. *1998 ASME International Mechanical Engineering Congress and Exposition*, Atlanta, GA, 1998.

(13) Bianchi, F.; Ferrigno, A.; Girault, H. H. *Anal. Chem.* **2000**, *72*, 1987–1993.

(14) Ermakov, S. V.; Jacobson, S. C.; Ramsey, J. M. *Anal. Chem.* **1998**, *70*, 4494–4504.

(15) Ermakov, S. V.; Jacobson, S. C.; Ramsey, J. M. *Anal. Chem.* **2000**, *72*, 3512–3517.

sample-focusing conditions may not be the most suitable for detection purposes.<sup>14,15</sup> Simulation of simple flow<sup>16</sup> and flow injection<sup>17</sup> in microsystems has also been carried out. For example, van Akker and co-workers studied the convection and diffusion phenomenon in a microflow injection system.<sup>18,19</sup> They also investigated the effects of continuous, pulsed, and stopped flow on the dispersion of a sample in a microfluidic T-injection system.<sup>20</sup> A calculation pointed out that one could reduce the so-called Taylor dispersion of the pressure-driven flow by modifying the shape of the cross section of the microchannel.<sup>21</sup>

In the present work, a numerical simulation based on the geometry used in a previous experimental work<sup>22</sup> has been performed. The experimental results suggested that the pinch condition has an effect on the detection of the analytes, but a systematic optimization proved difficult. To design an efficient setup, the effects of the following parameters on the detected signal for a pressure-driven flow have been investigated: the magnitudes of the velocity in the separation and injection channels, the presence of a sample pullback (during the separation process), the position and size of the detecting probe, and the width of the injection channel. The results show that the optimization of these parameters enables a good quality of the detected signal.

## THEORY

The following assumptions are made in the simulations:

(i) A two-dimensional model was used (see Figure 1) to simplify the simulation and decrease the calculation time (for a given precision of the results). This assumes that the depth of the channel is much larger than its width so that the velocity gradient in the third dimension (i.e., in the  $z$  direction far from the walls) can be neglected. In this case, in most parts of the depth of the channel, the flow velocity is limited only by the friction of the nearest walls ( $\partial V/\partial y$  gradient). In other words, the walls defining the depth are too far from each other (compared to the channel width) to have a pronounced influence on the core of the flow. This 2D model can be considered as a first approach to show the phenomena in the plane where the pinched injection is performed, even if it is clear that in most of the practical cases, the third dimension effect is not negligible.

(ii) The solution is sufficiently diluted to assume that the variations of the concentration do not modify the viscosity and the density of the fluid, which are also assumed to be uniform.

(iii) The flow switch is assumed to be instantaneous (hydrodynamic transient regimes are neglected).

(iv) The channel walls are assumed to be smooth, and the wall capillary forces are neglected.

For an incompressible fluid submitted to a laminar flow in a longitudinal channel (no gravity effect), the Navier–Stokes equation (eq 1) and the continuity equation (eq 2) can be written as

$$\rho \frac{\partial \mathbf{V}}{\partial t} + \rho \mathbf{V} \cdot \nabla \mathbf{V} = -\nabla p + \mu \nabla^2 \mathbf{V} \quad (1)$$

$$\nabla \cdot \mathbf{V} = 0 \quad (2)$$

where  $\mathbf{V}$  is the fluid velocity vector;  $p$ , the pressure;  $\rho$ , the density;  $\mu$ , the dynamic viscosity of the fluid; and  $t$ , the time. The magnitude of  $\mathbf{V}$  is given by  $V$ . For the following study, these equations are solved in a steady-state regime. The characteristic Reynolds number range used for the injection process is from 0.05 to 0.13. Because of the hypothesis (ii), the conservation of the species (eq 3) can be treated separately,

$$\frac{\partial c}{\partial t} + \mathbf{V} \cdot \nabla c - D \nabla^2 c = 0 \quad (3)$$

where  $c$  is the concentration of the species, and  $D$  is its molecular diffusion coefficient, which is also assumed to be uniform. The corresponding Peclet number (based on the channel width  $w$ ) is ranging from 50 to 130 (when the ratio  $V_0/V_1 = 16$ ). In a 2D channel, corresponding to a laminar flow between two parallel plates (Poiseuille or Hagen-Poiseuille profile), the average velocity is expressed as

$$\bar{V} = \frac{2}{3} V_{\max} \quad (4)$$

where  $V_{\max}$  is the maximal velocity value in the middle width of the microchannel. This velocity profile is introduced at the inlets of the channel.

For the simulations of the electroosmotic flow (EOF), the Navier–Stokes equation is written as

$$\rho \frac{\partial \mathbf{V}}{\partial t} + \rho \mathbf{V} \cdot \nabla \mathbf{V} = -\nabla p + \mu \nabla^2 \mathbf{V} + \rho_e \mathbf{E} \quad (5)$$

where  $\rho_e$  is the electrical charge density near the wall, and  $E$  is the electric field. In the following EOF calculations, the driving force ( $\rho_e \mathbf{E}$  term) is introduced by way of boundary conditions concerning the flow velocity at the walls. In this case, we assume that the characteristic channel dimension is much larger than the Debye layer scale.<sup>14,23</sup> Following the potential distribution in the cross channels corresponding to the literature (potential isovalues<sup>15</sup>), we assume that the electrical field,  $\mathbf{E}$ , is constant in each channel (even near the cross in our simulations). Results of Figure 7 show that this assumption is justified. As ref 15 states, we also assume that the conductivity of the solution is uniform ( $\sigma = \sigma_{\text{buffer}} = \text{constant}$ ). This last assumption allows us to use the Kirchhoff's law to establish the distribution of the electric field, leading to the wall velocity distribution in the different channels of the cross. Due to the flat profile of EOF, the velocity value is chosen to ensure the same flow rate as for the pressure-driven flow (PDF), which is expressed by

(16) van Kuijk, J. C. C. Ph.D. Thesis, University of Twente, 1997.

(17) van Akker, E. B.; Bos, M.; van den Berg, A.; van der Linden, W. E. *Anal. Methods Instrum.* **1996**, 251–253.

(18) van Akker, E. B.; Bos, M.; van der Linden, W. E. *Anal. Chim. Acta* **1998**, 373, 227–239.

(19) van Akker, E. B. Ph.D. Thesis, University of Twente, 1999.

(20) van Akker, E. B.; Bos, M.; van der Linden, W. E. *Anal. Chim. Acta* **1999**, 378, 111–117.

(21) Dutta, D.; Leighton, D. T. *Anal. Chem.* **2001**, 73, 504–513.

(22) Bai, X.; Lee, H. J.; Rossier, J. S.; Reymond, F.; Schafer, H.; Wossner, M.; Girault, H. H. *Lab Chip* **2002**, 1, 45–49.

(23) Patankar, N. A.; Hu, H. H. *Anal. Chem.* **1998**, 70, 1870–1881.

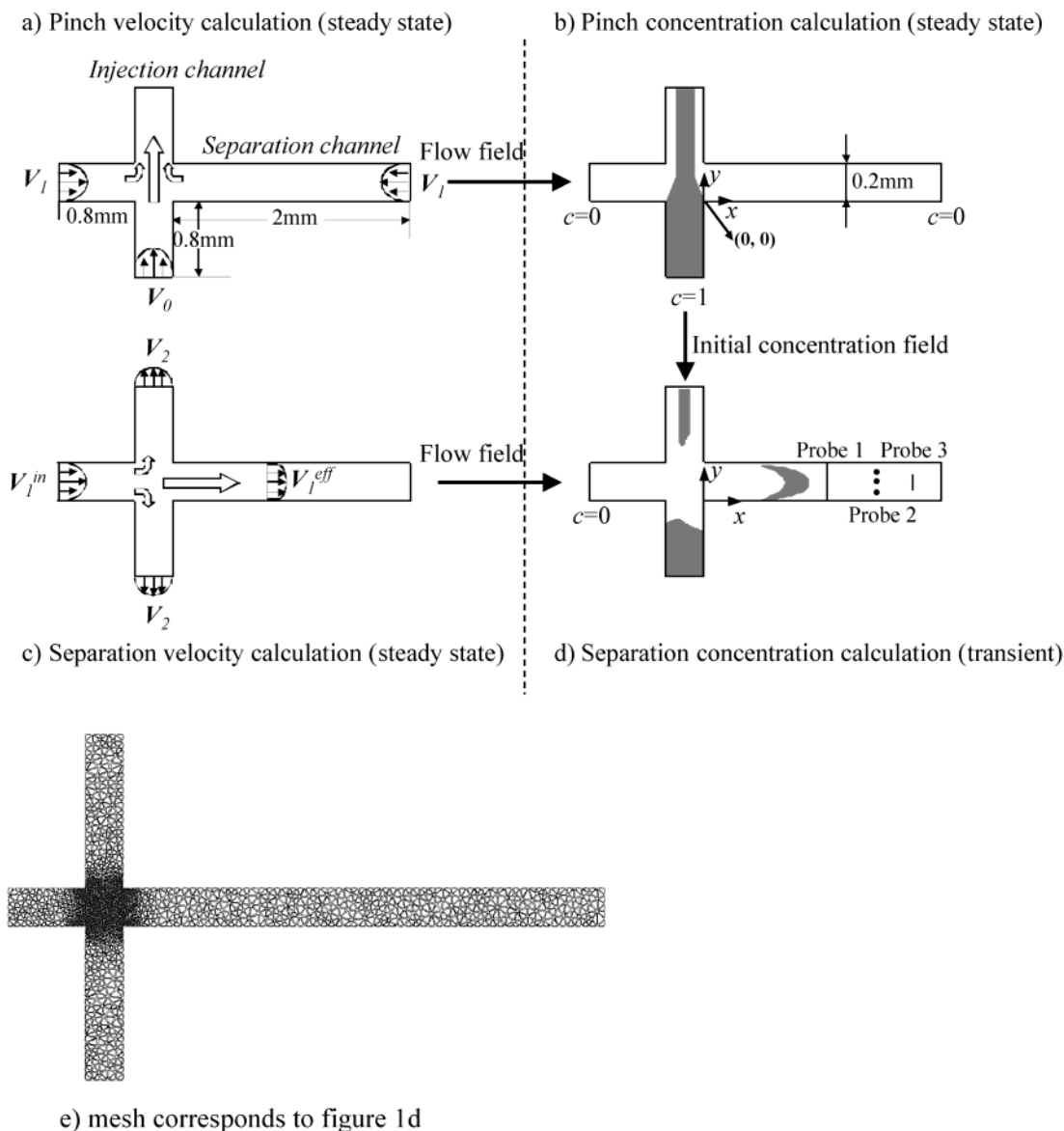


Figure 1. Methodology of the simulation in terms of calculation steps, boundary conditions, and initial conditions. The illustrated velocity profile corresponds to the pressure-driven flow calculations. For the EOF studies, flat profiles are imposed at the inlets, and the flow velocity at the walls is imposed instead of the no-slip condition. It is assumed that the depth of the channel is much larger than its width (i.e.,  $\Delta z \gg \Delta y$ ). Figure 1e shows the optimized mesh used for the last separation concentration transient calculation.

$$\bar{V}^{\text{EOF}} = \bar{V}^{\text{PDF}} = \frac{2}{3} V_{\text{max}}^{\text{PDF}} \quad (6)$$

In the following part, when not precised,  $V$  represents the maximum value of the pressure-driven flow velocity profile ( $V_{\text{max}}^{\text{PDF}}$ ).

**Geometries and Numerical Parameters.** All of the simulations have been carried out using the numerical software Flux-Expert (Simulog)<sup>24</sup> based on the finite element method. As explained before and illustrated in Figure 1a,c, the two velocity fields are calculated in a first step and used as input parameters for the concentration calculations (Figure 1b,d). A nonlinear steady-state algorithm is used for the hydrodynamic calculations, and a linear one is used for the determination of the concentration

profile. For nonlinear calculations, the convergence criterion is fixed at 0.5% for each unknown ( $V_x$ ,  $V_y$ , and  $p$ ). Both algorithms are based on the Gauss inversion method. In this work, the equations (1–3) are solved in a Cartesian two-dimensional form using a Silicon Graphics Indigo 2 workstation.

The studied model is based on the cross geometry shown in Figure 1. The two 200- $\mu\text{m}$ -wide microchannels are perpendicular to each other and are termed the separation (also called main channel corresponding to the  $x$  direction) and injection channels (also called sample channel or loading channel corresponding to the  $y$  direction), respectively. Although no separation is presented in this work, the term “separation channel” is used here for clarity purposes. The depths of the channels are much larger than their width so that the velocity gradient in the “ $z$ ” direction can be neglected.

(24) Simulog: 35 Chemin du Vieux Chêne, 38240 Meylan Zirst, France, anne-marie.bernier@simulog.fr.

Table 1. Main Flow Velocity Values Used in the Pressure-Driven Flow Simulations

| parameter    | values         | reference |
|--------------|----------------|-----------|
| $V_1$ (mm/s) | 0.04, 0.1, 1   | 0.1       |
| $V_0/V_1$    | 0.25, 1, 4, 16 | 4         |
| $2V_2/V_1$   | 0, 20, 40, 90% | 20%       |

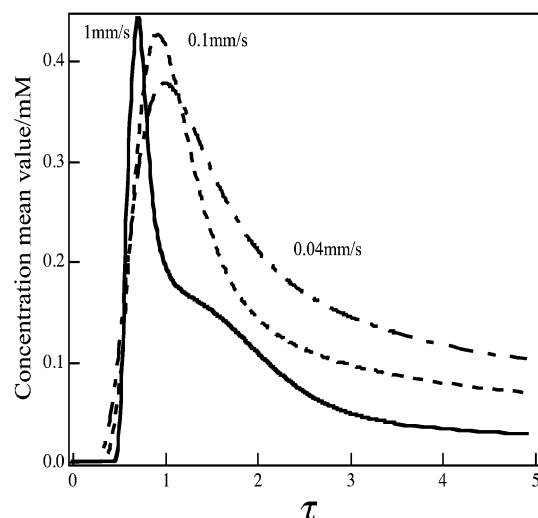


Figure 2. Effect of  $V_1$  on the time evolution of the integrated concentration on probe 1 (a transversal path from (500, 0) mm to (500, 200)  $\mu\text{m}$ ). Conditions:  $V_0/V_1 = 4$ , and  $V_2 = 0$ . Time is normalized by the flow velocity; see eq 7.

This process includes two steps, namely pinch (Figure 1a,b) and separation (Figure 1c,d). The final purpose of these simulations is to investigate the transient concentration evolution during the separation step (Figure 1d) in order to analyze the shape of the detection peak at the probe position. As mentioned before, two necessary items are needed for this final calculation: the fluid velocity field (Figure 1c) and the initial concentration condition (Figure 1b). As shown in Figure 1, the results are obtained in four steps: pinch velocity calculation; pinch concentration calculation; separation velocity calculation and separation concentration calculation. Only the last one is solved in a transient form.

As shown in Figure 1b, the origin, (0, 0), is fixed just after the cross, at the beginning of the effective separation channel. As shown in Figure 1d, three probes are employed as detectors to evaluate the signal. Probe 1 presents a transversal integration path in the separation channel from point (x, 0) to point (x, 200)  $\mu\text{m}$ . Probe 2 corresponds to a given point at different transversal positions in the separation channel. Probe 3 presents a transversal integration path (with different lengths) that are all centered at point (500, 100)  $\mu\text{m}$ .

As illustrated in Figure 1a, two reference velocities are introduced from the outlets of the channels in the pinch step: the sample velocity  $V_0$  and the pinch velocity  $V_1$ . These two parameters represent the maximum value of the velocity profile corresponding to the pressure-driven flow ( $V_{\text{max}}$ , eq 4). The corresponding parabolic velocity profiles are imposed as  $V_1$  boundary conditions at both ends of the separation channel, and the  $V_0$  profile is imposed at the sample inlet. The imposed  $V_0$  "pushes" the sample solution into the injection channel and  $V_1$  "drives" the eluent solution from both sides of the separation channel to the upper

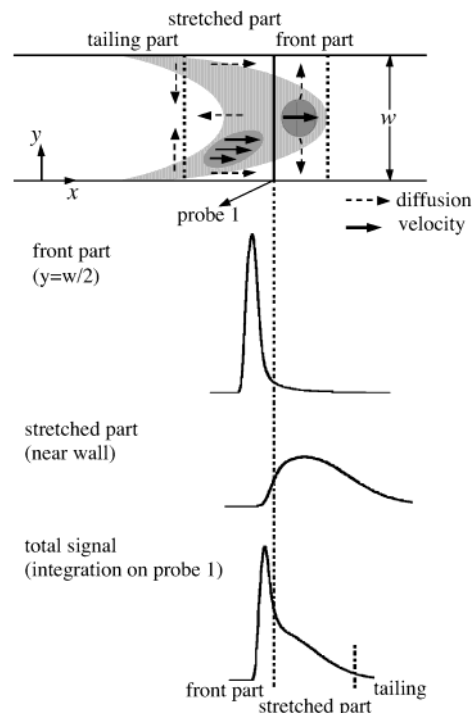


Figure 3. Schematic illustration of the formation of the double-humped peak at high magnitude of  $V_1$ . The signals given by the front and stretched parts correspond to the time evolutions of the local concentration distribution on probe 2 (placed in the middle width and near wall respectively). The total signal is integrated on probe 1, as for Figure 2. A 20% pullback velocity was chosen to reduce the sample leakage (and its contribution in the tailing). Full arrows represent the velocity vector. Dashed arrows represent diffusion vectors.

injection channel. The sample solution is pinched at the cross intersection by the eluent flow ( $V_1$ ), leading to a trapezoidally shaped plug shown in Figure 1b. For the separation step (Figure 1c), a third velocity profile ( $V_{\text{max}}$ ,  $V_2$ ) is introduced at the outlets of the injection channel to induce a pullback of the sample solution.<sup>22</sup> Then,  $V_1$  is used to impose the separation velocity. Indeed, to be consistent with the experiment,<sup>22</sup> in the remainder of the paper (except notation), we use the same value for  $V_1$  during the pinch and separation steps at the eluent solution inlet. As a consequence, the magnitude of  $V_1$  in the separation step is subdivided into 2 velocity values named input separation velocity  $V_1^{\text{in}}$  in the separation channel before the cross and effective separation velocity,  $V_1^{\text{eff}}$ , after the cross. The trapezoidally shaped sample plug will be driven into the separation channel, whereas the pullback velocity,  $V_2$ , decreases the diffusion of the species remaining in the injection channel. From the description above, it is clear that this pinch injection principle is exactly the same as the electrokinetic pinch injection.<sup>15</sup>

For all the pressure-driven flow calculations, the velocity boundary condition on the walls is fixed at 0 (no slip condition). For the pinch concentration calculation, the boundary concentration is 1 mM at the sample inlet and 0 at the eluent inlet (see Figure 1b). For the separation concentration calculation step, the boundary concentration at the eluent inlet is 0. The velocity parameters used are listed in Table 1. The diffusion coefficient  $D$  of the fluid is  $10^{-9} \text{ m}^2 \text{ s}^{-1}$ , the viscosity is  $10^{-6} \text{ m}^2 \text{ s}^{-1}$ , and the density is  $10^3 \text{ kg m}^{-3}$ . The time step used was 0.25 ms (error <1%),

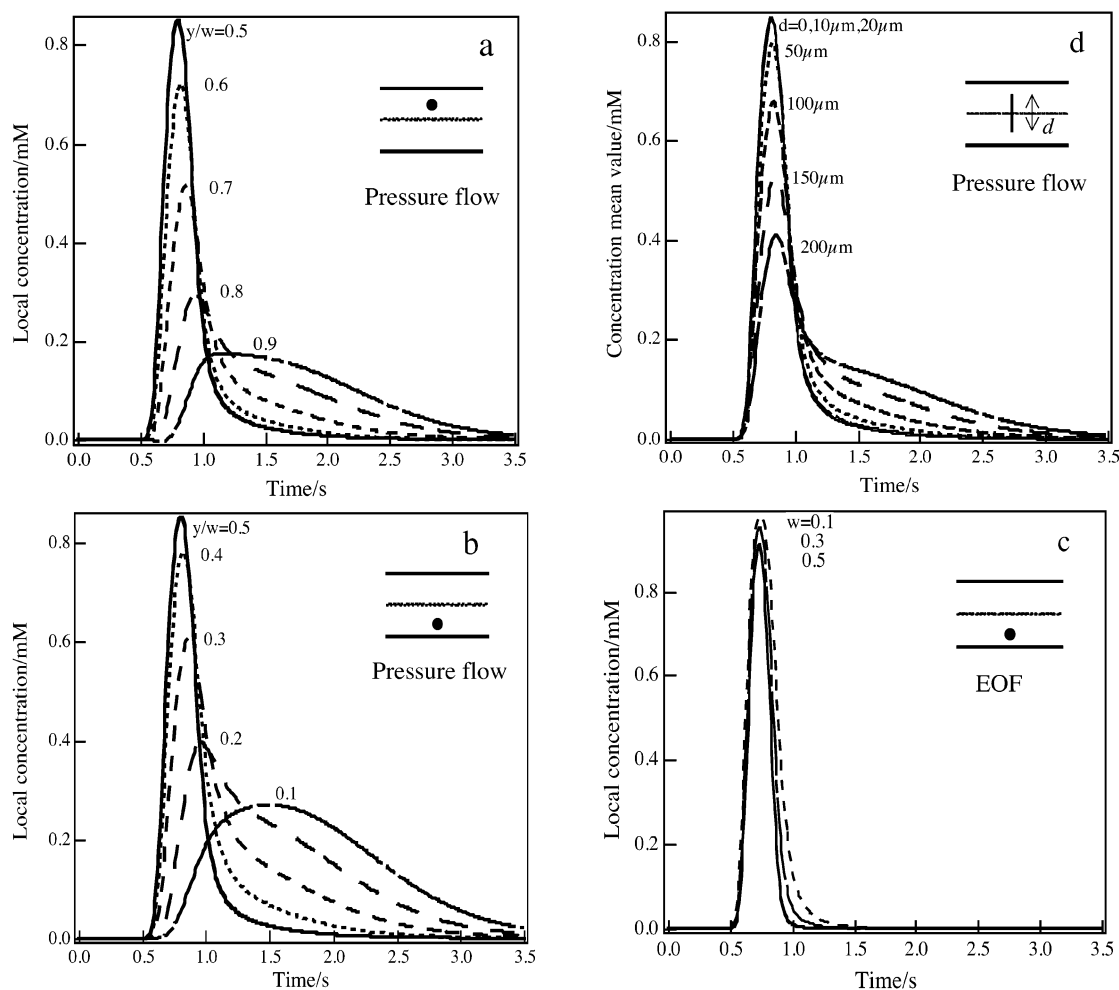


Figure 4. Time evolution of the local concentration distribution on different probe 2 transversal positions (a, b, and c).  $w$  is the width of the separation channel,  $y$  is the absolute transversal ordinate of the detecting probes, the longitudinal position of which is fixed at  $500\ \mu\text{m}$  after the injection cross. Figure 4a and b presents the signal for the probe positions above and below the middle width of separation channel ( $y/w \geq 0.5$  and  $y/w \leq 0.5$ ), respectively. Figure 4c presents the same process with the EOF pinch injection (the probe transversal positions are below the middle of the separation channel). Conditions:  $V_1 = 1\ \text{mm/s}$  for pressure flow ( $\bar{V} = 0.67\ \text{mm/s}$  for both flows),  $V_0/V_1 = 4$ , and  $2V_2/V_1 = 20\%$ . Figure 4d presents the effect of the transversal integration length (d) of probe 3.

and an optimized mesh (as shown in Figure 1e,  $40\ \mu\text{m}$  in the channel and  $10\ \mu\text{m}$  at the center of the cross) was used for the last separation concentration calculation step. The choice of time step and mesh was the result of a careful calibration and error evaluation, as described in the Supporting Information.

## RESULTS AND DISCUSSION

**Effect of the Separation Velocity.** Figure 2 shows the time evolution of the concentration at  $x = 0.5\ \text{mm}$  after the cross for different magnitudes of  $V_1$ . The concentration is integrated along probe 1. To enable the comparisons between results obtained with different residence times, the nondimensional time,  $\tau$ , is introduced.

$$\tau = \frac{V_1 t}{x_c} \quad (7)$$

The characteristic length value chosen here for  $x_c$  is  $1\ \text{mm}$ . In the case of a high velocity value ( $V_1 = 1\ \text{mm/s}$ ), one can verify

that the time of arrival of the species at probe 1 is  $0.5$ , corresponding to the probe distance after the cross ( $0.5\ \text{mm}$ ). As can be seen in Figure 2, the sensitivity is increased with a higher magnitude of  $V_1$ , and the peak is narrower. At a low velocity value ( $0.04\ \text{mm/s}$ ), the diffusion effect dominates over convection simply because of a longer diffusion time. Therefore, the peak is broader with more serious tailing due to the “leakage” of the species remaining in the injection channel. At a high velocity ( $1\ \text{mm/s}$ ), the diffusion time is reduced, and a sharper signal is observed with a double-humped peak.<sup>25</sup> The influence of the diffusion coefficient  $D$  on the detected peak shape<sup>19</sup> must be noted here. By increasing  $D$ , the double-humped peak shape can be avoided because of the diffusion dominant mechanism. To analyze this peak shape in detail, we will look at the local signal along this transversal probing path (probe 2 as shown in Figure 1d).

**Transversal Probe Position.** The above-mentioned phenomenon has already been observed and reported in the literature.<sup>19,25</sup>

(25) Vanderslice, J. T.; Rosenfeld, A. G.; Beecher, G. R. *Anal. Chim. Acta* **1986**, *179*, 119–129.



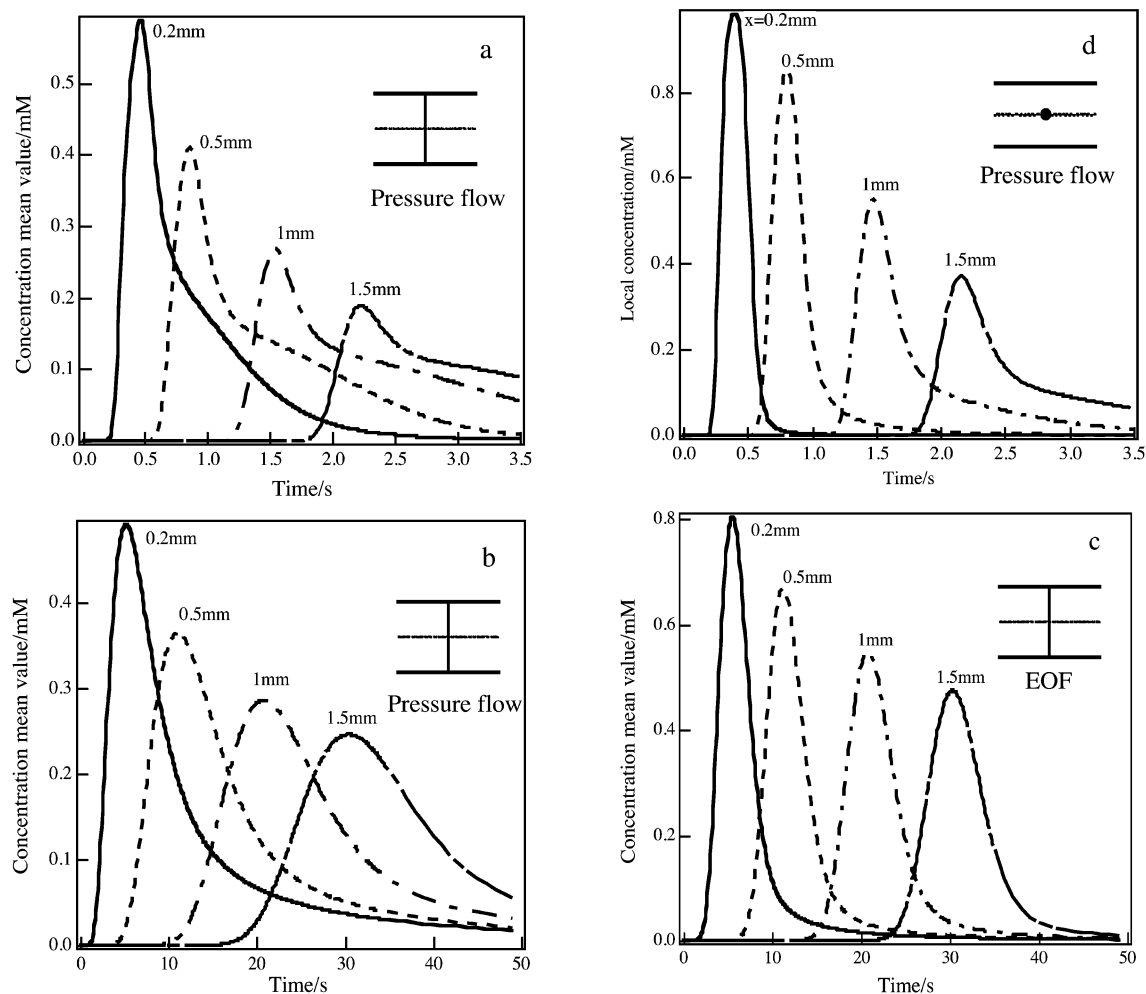


Figure 5. Time evolution of the concentration integrated on different probe 1 longitudinal positions from  $(x, 0)$  to  $(x, 200) \mu\text{m}$ .  $x$  is the absolute longitudinal position of probe 1, that is, 0.2, 0.5, 1, and 1.5 mm. Conditions:  $V_0/V_1 = 4$ , and  $2V_2/V_1 = 20\%$  (a) pressure-driven flow,  $V_1 = 1 \text{ mm/s}$ ; (b) pressure-driven flow,  $V_1 = 0.1 \text{ mm/s}$ ; (c) EOF pinch injection, the average velocity is same as (b),  $\bar{V} = 0.067 \text{ mm/s}$ ; (d) pressure-driven flow, the same sequence of the concentration profiles on probe 2,  $(x, 100) \mu\text{m}$ .

Figure 3 explains the details of the detection sequence of this peak. Under the pressure-driven flow profile, the initial pinched sample plug is stretched to assume a parabolic shape similar to the flow profile. From the detection point of view, the sample plug can approximately be divided into three parts: the front part, the stretched part, and the tailing part followed by the sample leakage from the injection channel. In the middle of the channel, the species are transported at the maximum velocity and arrive first at probe 1 (front part). As a consequence, they have the shortest time of diffusion when detected and form the most concentrated zone, explaining the high value of their peak contribution. The second part arriving at the probe 1 is the "stretched" middle part of the sample plug. This part is strongly influenced by the velocity gradient, inducing a long distribution of arrival time at the probe 1 and a broad signal peak. After that, one can observe the tailing due to the near-wall contribution followed by the sample leakage from the injection channel. To verify this description, the detection point (probe 2) is placed along probe 1 path at different transversal positions. The local concentration evolutions on those points are shown in Figure 4. The two graphs, Figure 4a,b, present the upward ( $100 \mu\text{m} = y < 200 \mu\text{m}$ ) and downward ( $0 < y = 100 \mu\text{m}$ ) parts of the channel,

respectively. The difference between them is due to the trapezoidal shape of the initial pinched sample shape. When probe 2 is near the middle of the microchannel ( $0.3 < y/w < 0.7$ , where  $w$  is the width of the separation channel, i.e.,  $200 \mu\text{m}$ ), the detection signal has the best quality, because the probe essentially detects the front part of the sample plug without any significant diffusion and velocity gradients. When probe 2 is closer to the wall ( $y/w = 0.1$  or  $0.9$ ), the local velocity is much lower; the peak is broadened and the arrival time is delayed, as shown in Figure 4a,b. Between these characteristic  $y$  values (near the center or near the wall), a mixture of the two shapes can be found at probe positions of  $y/w = 0.2$  and  $0.8$ . Consequently, it leads to a double-humped peak, as observed on probe 1 in Figure 2 (high magnitude of  $V_1$ ). At a lower magnitude of  $V_1$ , the solution has more time to diffuse in the  $(x, y)$  plane. In this case, the transversal component of the diffusion compensates for the lateral stretching of the plug, leading to a cancellation of the progressive delay of the arrival time.

The local concentration evaluations corresponding to the EOF simulations are shown in Figure 4c under the same conditions. As expected, a quasi-uniform peak distribution is observed along the  $y$  direction as a result of the flat flow profile in EOF conditions.

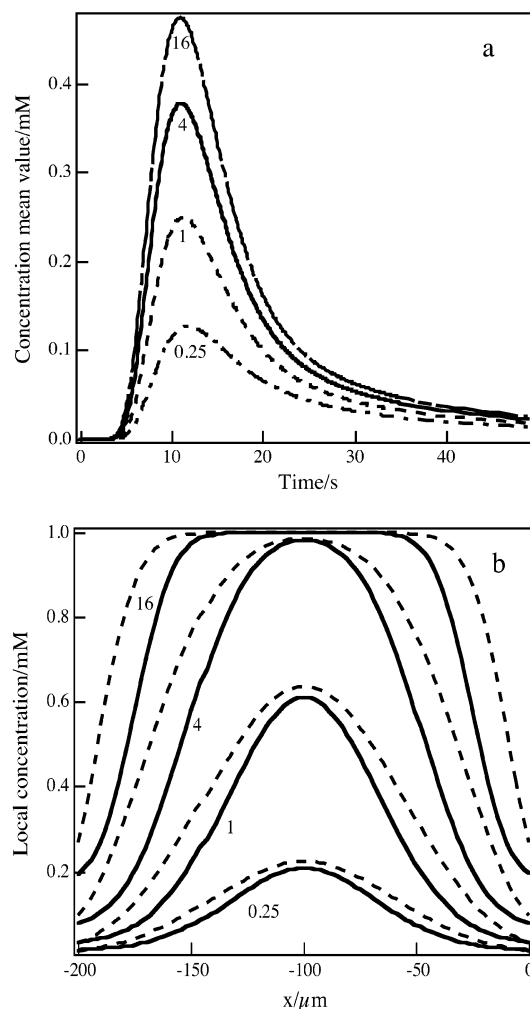


Figure 6. Effect of the sample velocity ratio  $V_0/V_1$ .  $V_1 = 0.1$  mm/s and  $2V_2/V_1 = 20\%$ . Figure 6a presents the concentration evolutions at different ratios of  $V_0/V_1$ , that is, 0.25, 1, 4, and 16. The concentration is integrated on probe 1, a transversal path from (500, 0) to (500, 200)  $\mu\text{m}$ . Figure 6b shows the comparison between the pressure pinch (solid line) and the electrokinetic pinch (dashed line) on a longitudinal path (at the edge of the cross intersection, from (−200, 200) to (0, 200)  $\mu\text{m}$ ).

The minor differences between those signals are due to the trapezoidal shape of the original pinched sample plug.

From the discussion above, it is evident that the middle of the channel is the best position for detection when it is sufficiently close to the injection cross, regardless of the magnitude of  $V_1$ . It can be realized by a proper detection technique, such as focusing a confocal microscope on a spot located in the middle of the channel.<sup>26</sup> Figure 4d shows the concentration evolution on probe 3, where the concentration is integrated on different transversal paths that are all centered at point (500, 100)  $\mu\text{m}$  in the separation channel. The lengths of probe 3 range from 0 to 200  $\mu\text{m}$ . When the path length is 0, probe 3 actually becomes probe 2 in the middle of the separation channel and it sees only the most concentrated sample core (the front part, as shown in Figure 3). When the path length is increased, probe 3 begins to see a more extended part of the plug from the center to the near-wall part. Until the path length reaches 50  $\mu\text{m}$ , there is only a very small

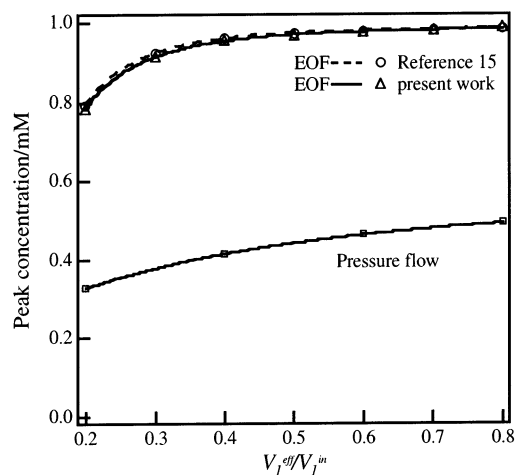


Figure 7. Effect of the pullback ratio on the peak value: calibration of the EOF calculations with the results of ref 15 and comparison between EOF and pressure-flow pinch injection. The concentration is integrated on a transversal path like probe 1 at 100  $\mu\text{m}$  downstream from the cross (from (100, 0) to (100, 50)  $\mu\text{m}$ ) to have the concentration mean value at the peak time. Conditions: 50- $\mu\text{m}$  channel width for all the arms of the cross design, diffusion coefficient of  $3 \times 10^{-10}$   $\text{m}^2/\text{s}$ . The value of  $V_1^{\text{eff}}$  is fixed as 1.5 mm/s for EOF (corresponding to  $V_1 = 2.25$  mm/s for the pressure-driven flow),  $V_0/V_1^{\text{eff}} = 14/3$ . It is worth noting that  $V_1^{\text{eff}}/V_1^{\text{in}} = \epsilon_{4D}$ , where  $\epsilon_{4D}$  corresponds to the notation of ref 16 describing the ratio between the electric field values in the corresponding “effective” (after the cross) and “input” channels (before the cross).

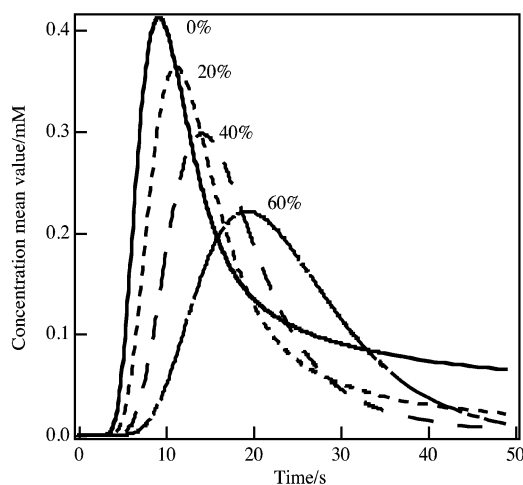


Figure 8. Effect of the pullback velocity  $V_2$  on the time evolution of the concentration integrated on probe 1 (the transversal path from (500, 0) to (500, 200)  $\mu\text{m}$ ).  $V_1 = 0.1$  mm/s,  $V_0/V_1 = 4$ . The curves correspond to different values of  $2V_2/V_1$ , that is, 0, 20, 40, and 60%.

decrease in the signal sensitivity. Even the integration of the half-width of the channel ( $d = 100$   $\mu\text{m}$ ) can avoid the double-humped shape of the signal, which appears at  $d = 150$   $\mu\text{m}$ . This result gives useful information on the resolution needed for the “spot” detection using a confocal microscope.

**Longitudinal Probe Position.** The aim of this part is to see the effect of the junction length between the cross injector and the following separation system. The transversal integration of the signal is shown in Figure 5 for different longitudinal positions of probe 1 ( $V_1 = 1$  and 0.1 mm/s in Figure 5a and 5b, respectively). The signal tends to be broader along the longitudinal position.

(26) Ocirk, G.; Tang, T.; Harrison, D. J. *Analyst* **1998**, *123*, 1429–1434.

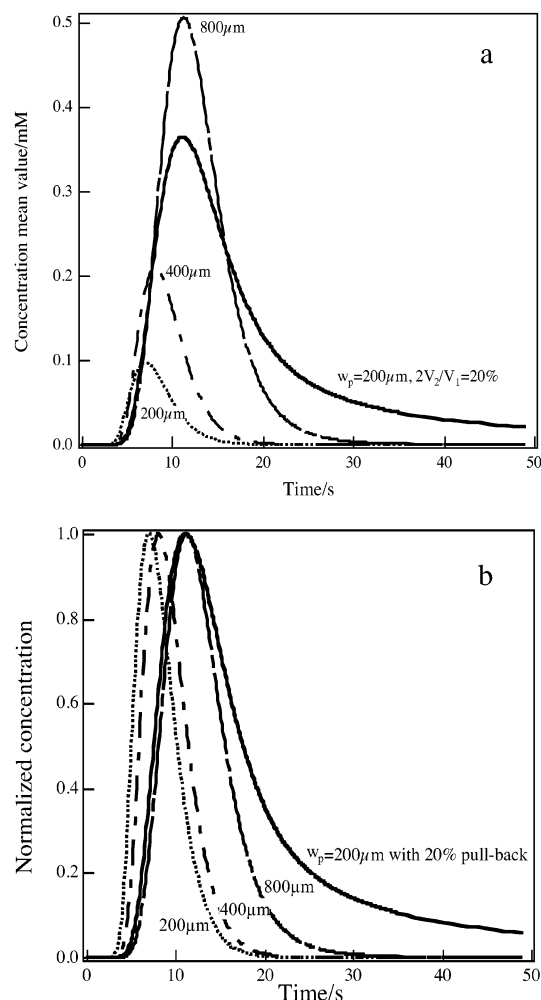


Figure 9. Effect of the width of the injection channel ( $w_p$ ) on the time evolution of the concentration integrated on probe 1. The solid line corresponds to the reference signal obtained in a 200- $\mu\text{m}$ -wide channel with 20% sample pullback velocity,  $V_1 = 0.1 \text{ mm/s}$ ,  $V_0/V_1 = 4$ . The dashed lines correspond to different injection channel widths with 90% sample pullback velocity.  $V_1^{\text{in}} = 1 \text{ mm/s}$ ,  $V_1^{\text{eff}} = 0.1 \text{ mm/s}$ , and  $Q_0/Q_1 = 4$ . Figure 9b presents the normalized peaks.

One can also consider it as the time evolution of the injected plug. From the detection point of view, the signal has better resolution when the detection window is close to the injection point. It is worth noting that the evolution of the plug at a medium magnitude of  $V_1$  (0.1 mm/s) is actually better than that at a higher one (see Figure 5b). The decrease of the peak height is smaller than that corresponding to a higher magnitude of  $V_1$  at the same position. As mentioned before, at high magnitude of  $V_1$  (1 mm/s), the front part (i.e., the most concentrated part) is very small, as compared to the whole plug. The dilution of this part by diffusion will therefore be more effective because of the increased surface-to-volume ratio. It explains the rapid decrease of the peak quality with the distance when the flow velocity is high (Figure 5a). This is another reason to choose a low magnitude of  $V_1$  (0.1 mm/s) in the following calculations.

The same integrated signal in EOF is shown in Figure 5c with a velocity magnitude of  $V_1 = 0.067 \text{ mm/s}$  (same average flow rate as for the pressure-driven flow). Enhanced peak resolution is observed compared to pressure flow. The time stability of the peak quality is improved, as expected.

Figure 4d shows that when probe 2 is placed in the middle of the separation channel, it results in a notably improved peak of the local concentration evolution. This rule is applied for a high value of  $V_1$  ( $V_1 = 1 \text{ mm/s}$ ) in pressure-driven flow, and the result is shown in Figure 5d. As expected, no double-humped peak is observed, and the signal has a better quality when close to the injection cross ( $x < 600\text{--}800 \mu\text{m}$ ). The decrease of the peak is more rapid, which confirms that the small front plug diffuses more quickly.

**Effect of the Sample Velocity,  $V_0$ .** The amount of injected sample is mainly governed by the value of  $V_0/V_1$ . Concerning the separation step, Figure 6a shows the time evolution of the concentration mean value (integrated on probe 1) with different ratios of  $V_0/V_1$ . Concerning the pinch step, Figure 6b shows the concentration distribution on a 200- $\mu\text{m}$  longitudinal path at the edge of the cross center,  $y = 200 \mu\text{m}$ . A high value of  $V_0/V_1$  (i.e., 16) leads to a larger amount of pinched sample at the cross (Figure 6b, solid line) and a higher detected signal, as shown in Figure 6a. On the other hand, for a low value of  $V_0/V_1$  (i.e., 0.25), the smaller amount of sample will be rapidly spread by diffusion (higher surface-to-volume ratio). Consequently, the height of the peak is strongly reduced, as compared with the sample leakage contribution to the signal.

The electrokinetic pinch and pressure pinch are compared in Figure 6b. If only the pinch efficiency is concerned, the pressure flow gives a more confined sample plug, as compared to EOF for the same flow rate. In EOF, the sample plug is 23% thicker than the one corresponding to the pressure flow pinch (for  $c = 0.5$ ).

A sharper pinch concentration profile could be obtained when the magnitudes of  $V_0$  and  $V_1$  are multiplied by a factor of 10. At a high velocity, the residence time is short, giving the species less time to diffuse. However, since the aim of a low velocity value is to avoid the double-humped peak obtained by the transversal integration of the signal, a low magnitude of  $V_1$  (0.1 mm/s) with a  $V_0/V_1$  value of 4 is used for the following simulations.

**Effect of the Pullback Velocity,  $V_2$ .** Decreasing  $V_1$  can improve the quality of the detected signal, as shown in Figure 2, but it also leads to a possible leakage of the sample from the injection channel. To minimize it, a pullback velocity,  $V_2$ , is introduced at the edges of the injection channel during the separation process, to push back this "bleeding part" of the sample in the injection channel. First, a comparison of the pullback effect between the EOF pinch injection and the pressure-flow pinch injection is presented in Figure 7. The same conditions as in ref 15 are used. The channel width is decreased to 50  $\mu\text{m}$ , the diffusion coefficient is  $3 \times 10^{-10} \text{ m}^2/\text{s}$ , and the signal is detected 100  $\mu\text{m}$  after the injection cross. In Figure 7, the ordinate in the  $y$  axis is the peak value of the concentration evolution (integrated on the transversal path of probe 1). When the pullback ratio is increased, the input velocity  $V_1^{\text{in}}$  is enhanced to maintain a constant value of the effective velocity  $V_1^{\text{eff}}$  in the separation channel. This enables keeping the same retention time and cancels the time diffusion effect in order to concentrate the study on the sample pullback effect. The comparison between literature values and the present work is also shown in Figure 7. The agreement



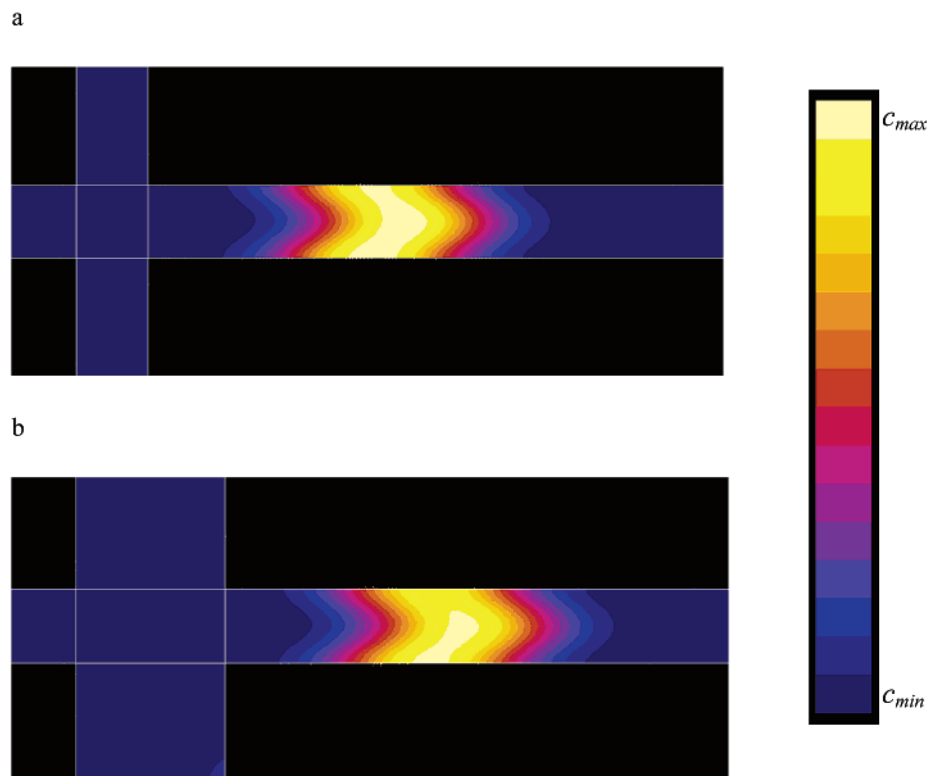


Figure 10. Concentration isovalues at 10 s for different injection channel widths. The pullback volumetric flow rate ratio is 90%. The window length shown is 2 mm. Different isovalues of maximum concentration are used in Figure 10a and 10b to emphasize the plug distribution. Conditions: (a)  $w_P = 200 \mu\text{m}$ ,  $C_{\text{max}} = 0.08 \text{ mM}$ ,  $V_0/V_1^n = 4$ ,  $V_1^{\text{eff}} = 0.1 \text{ mm/s}$ ; (b)  $w_P = 400 \mu\text{m}$ ,  $C_{\text{max}} = 0.2 \text{ mM}$ ,  $V_0/V_1^n = 2$ ,  $V_1^n = 1 \text{ mm/s}$ ,  $V_1^{\text{eff}} = 0.1 \text{ mm/s}$ .

is good, with a deviation between 0.1 and 1% (depending on  $V_1^{\text{eff}}$ ). As can be seen in Figure 7, both EOF and pressure-driven flow show the same tendency for the peak evolution with the pullback ratio. High sample pullback results in more sample being pushed back to the injection channel, and therefore, a lower concentration value can be observed. The maximum values of the pressure flow are much smaller than those of the EOF, mainly because of the small channel width and the high velocity value (2.25 mm/s corresponding to  $\bar{V}$  of 1.5 mm/s), which amplifies the stretching of the plug.

The results corresponding to the present geometry and conditions (shown in Figure 8) further confirm the results in Figure 7. The integrated concentration evolution (probe 1) for different values of the parameter  $2V_2/V_1$  (representing the fraction of the fluid dragged in both sides of the injection channel) is shown in Figure 8. As mentioned before, the input velocity,  $V_1^n$  is maintained constant. In the absence of sample pullback (0% curve), the sample plug is not sufficiently separated from the sample leakage in the injection channel (meaning more sample leakage and a bigger tail). As illustrated in Figure 8, the pullback effect on sample leakage can be pronounced. Compared to the absence of sample pullback, the peak-to-tail ratios at 50 s after injection are 17.3 and 48.1 for  $2V_2/V_1$  equal to 20 and 40%, respectively. However, when the magnitude of  $V_2$  is too high ( $>40\%$  of “lost” fluid), it actually decreases the effective velocity  $V_1^{\text{eff}}$  in the separation channel after the cross intersection, leading to a delay of the peak arrival time, a decreased sensitivity and a peak thickening (due to time and diffusion effects). When the sensitivity approaches the limiting value for the experimental design, the increase of the injection channel width may be of some help.

**Effect of the Injection Channel Width.** To follow the idea just mentioned above, the width of the injection channel ( $w_P$ ) is enlarged while a high sample pullback effect is maintained. Because of the section difference and in order to avoid a different pinch ratio, the characteristic pinch ratio is now established between the volumetric flow rates ( $Q_0/Q_1$ ) rather than the flow velocities. Therefore, for a 200- $\mu\text{m}$ -wide injection channel, the  $V_0/V_1$  value is equal to 4, whereas it is set to 2 and 1 for channels of 400 and 800  $\mu\text{m}$  width, respectively. The time evolutions of the concentration (integrated on probe 1) are compared for different injection channel widths, as shown in Figure 9a. The 90% pullback ratio is employed, and  $V_1^n$  is multiplied by 10, as compared with that of the last section (i.e.  $V_1$  is 1 mm/s) so that the effective velocity value in this channel is globally unchanged ( $V_1^{\text{eff}} = 0.1 \text{ mm/s}$ ). With 90% pullback velocity in the 200- $\mu\text{m}$  injection channel, most of the initial plug is driven into the transversal arms of the injection channel. Consequently, the peak tailing is completely removed, as shown in Figure 9, but the detection sensitivity is greatly reduced. When the injection channel width is increased, the peak value is notably increased while keeping a good peak resolution, which is confirmed by the plug shapes shown in Figure 10. Indeed, when increasing this width from 200 to 400  $\mu\text{m}$ , the maximum concentration of the plug is multiplied by 3 while its relative thickness is maintained constant. When using an 800- $\mu\text{m}$  injection channel (Figure 9a), the signal observed is higher than the reference one (200  $\mu\text{m}$  with 20% pullback velocity), even with 90% pullback velocity, and the tailing is efficiently canceled by this high sample pullback. Comparing the cases with 90% pullback velocity, the sensitivity of the signal is increased by 500% when going from a 200- $\mu\text{m}$  to

an 800- $\mu\text{m}$  injection channel. Meanwhile, a good peak resolution is maintained, as shown in Figure 9b (normalized peak intensities).

## CONCLUSION

Computer simulation of pressure-driven injections operated in a channel having a cross geometry has identified a set of running parameters that provides improved detection signal. Once optimized, pressure-pinch injection can be an alternative to EOF in situations when control of the surface charge (and the reproducibility of the flow) is difficult to achieve. This drawback is particularly evident in chip immunoassay, which relies on protein adsorption and surface modifications. It has been found that the effective separation flow rate,  $V_1^{\text{eff}}$  (after the cross intersection), contributes mostly to the quality of the final detection signal. A high value of  $V_1^{\text{eff}}$  may not be beneficial for detection purposes, because of the presence of the so-called double-humped peak when the concentration evolution is transversally integrated into the channel. Nevertheless, this problem can be overcome by using another detection technique (for instance, using a confocal microscope) that enables focalizing the detection at the center of the channel.

It has been found that, as for the electrokinetic pinch injection,<sup>15</sup> a tight pinch is not favorable, because it leads to a high leakage level and a low sensitivity (due to the low ratio between the sample band thickness and the injection channel width). A high sample pullback (for example, 90%), coupled with a sufficient  $V_1^{\text{eff}}$ , could remove the sample leakage effect and enhance the peak resolution (and the selectivity), but the sensitivity would be notably decreased. To increase this sensitivity while keeping the advantage of high sample pullback, an enlarged injection channel width can be used.

## APPENDIX

The Cartesian 2D numerical formulation is here described for the Navier–Stokes and convection–diffusion equations, corresponding to available equations in the Flux-Expert software database. The convection–diffusion eq 3 is here written in its general local form.

$$\frac{\partial c}{\partial t} + \nabla \cdot (-D\nabla c + \mathbf{V}c) = 0 \quad (\text{A1})$$

**Integral Form.** This form is derived by using the Galerkin's formulation (multiplication by a projective function  $\alpha$  and integration on the domain of study,  $\Omega$ ).

$$\int_{\Omega} \alpha \left[ \frac{\partial c}{\partial t} + \nabla \cdot (-D\nabla c + \mathbf{V}c) \right] d\Omega = 0 \quad (\text{A.2})$$

The derivation of the convection term (see eq A.4) is simplified by taking into account the continuity equation  $\nabla \cdot \mathbf{V} = 0$ . By decomposing the product between  $\alpha$  and the divergence, the second-order derivative becomes using eq A.3 (integration by

$$\alpha \nabla \cdot (-D\nabla c) = \nabla \cdot (-\alpha D\nabla c) + D\nabla \alpha \cdot \nabla c \quad (\text{A.3})$$

parts) and the Ostrogradsky theorem, eq A.2 leads to eq A.4 under the assumption that no flux crosses the boundaries of the domain.

$$\int_{\Omega} \alpha \left[ \frac{\partial c}{\partial t} + D\nabla \alpha \cdot \nabla c + \alpha \nabla \cdot \mathbf{V}c \right] d\Omega = \int_{\partial\Omega} \alpha D \frac{\partial c}{\partial n} \cdot d\mathbf{l} = 0 \quad (\text{A.4})$$

To obtain the matrix form, the unknown  $c$  is discretized on the nodes of the domain by means of an interpolation function of the same type as the projective function (second-order polynomial function). The decomposition of the scalar products of eq A.4 on the  $(x, y)$  coordinates is not detailed here, but this is done for the following hydrodynamic equations to be more explicit.

The Navier–Stokes and continuity equations (eqs 1, 2) are expressed in local form for steady-state conditions (the gravity term is not taken into account here)

$$\begin{aligned} \rho V_x \frac{\partial V_x}{\partial x} + \rho V_y \frac{\partial V_x}{\partial y} = \\ - \frac{\partial p}{\partial x} + \frac{\partial}{\partial x} \left( 2\mu \frac{\partial V_x}{\partial x} \right) + \frac{\partial}{\partial y} \left( \mu \frac{\partial V_x}{\partial y} \right) + \frac{\partial}{\partial y} \left( \mu \frac{\partial V_y}{\partial x} \right) \end{aligned} \quad (\text{A.4})$$

$$\begin{aligned} \rho V_x \frac{\partial V_y}{\partial x} + \rho V_y \frac{\partial V_y}{\partial y} = \\ - \frac{\partial p}{\partial y} + \frac{\partial}{\partial x} \left( \mu \frac{\partial V_x}{\partial y} \right) + \frac{\partial}{\partial x} \left( \mu \frac{\partial V_y}{\partial x} \right) + \frac{\partial}{\partial y} \left( 2\mu \frac{\partial V_y}{\partial y} \right) \end{aligned} \quad (\text{A.5})$$

$$\frac{\partial V_x}{\partial x} + \frac{\partial V_y}{\partial y} = 0 \quad (\text{A.6})$$

These local equations are projected (i) on second-order polynomial functions  $\alpha$  for eqs A.4 and A.5 (ii) on first-order polynomial functions  $\beta$  for (A.6). Integration on the domain of study and integration by parts of the second-order derivatives give

$$\begin{aligned} \int_{\Omega} \left[ \alpha \rho V_x \frac{\partial V_x}{\partial x} + \alpha \rho V_y \frac{\partial V_x}{\partial y} - \frac{\partial \alpha}{\partial x} p + \right. \\ \left. 2\mu \frac{\partial \alpha}{\partial x} \frac{\partial V_x}{\partial x} + \mu \frac{\partial \alpha}{\partial y} \frac{\partial V_x}{\partial y} + \mu \frac{\partial \alpha}{\partial y} \frac{\partial V_y}{\partial x} \right] dx dy = 0 \end{aligned} \quad (\text{A.7})$$

$$\begin{aligned} \int_{\Omega} \left[ \alpha \rho V_x \frac{\partial V_y}{\partial x} + \alpha \rho V_y \frac{\partial V_y}{\partial y} - \frac{\partial \alpha}{\partial y} p + \right. \\ \left. \mu \frac{\partial \alpha}{\partial x} \frac{\partial V_x}{\partial y} + \mu \frac{\partial \alpha}{\partial x} \frac{\partial V_y}{\partial x} + 2\mu \frac{\partial \alpha}{\partial y} \frac{\partial V_y}{\partial y} \right] dx dy = 0 \end{aligned} \quad (\text{A.8})$$

$$\int_{\Omega} \beta \rho \left[ \frac{\partial V_x}{\partial x} + \frac{\partial V_y}{\partial y} \right] dx dy = 0 \quad (\text{A.9})$$

The matrix form is finally obtained by discretization of the unknown on the  $\alpha$  polynomial function (for  $V_x$  and  $V_y$ ) and on the  $\beta$  ones (for the pressure). Cuthill MacKee node renumbering is used to reduce the calculation time. To avoid problems of matrix singularity, the pressure is introduced in the continuity equation (A.9) by using a penalty method ( $\nabla \cdot \mathbf{V} = \epsilon p$ ), where  $\epsilon$  is the subparametric penalty coefficient. Its value ( $10^{-14}$  in Cartesian coordinates) is verified to be sufficiently small not to affect the flow rate conservation.

#### ACKNOWLEDGMENT

The authors thank Jacques Morandini (Simulog), Metrohm (CH) and the Swiss Commission for Technology and Innovation (CTI), and the fifth European Union Framework Research Program QLG2-CT-2001-01903/OFES 01.0182-2 "MicroProteoMics" for financial support.

#### SUPPORTING INFORMATION AVAILABLE

Details of the calibration of the numerical model. This material is available free of charge via the Internet at <http://pubs.acs.org>.

Received for review July 5, 2002. Accepted October 2, 2002.

AC025920+